

High-Performance Flexible Transparent Electrode with an Embedded Metal Mesh Fabricated by Cost-Effective Solution Process

Arshad Khan, Sangeon Lee, Taehee Jang, Ze Xiong, Cuiping Zhang, Jinyao Tang, L. Jay Guo, and Wen-Di Li*

A new structure of flexible transparent electrodes is reported, featuring a metal mesh fully embedded and mechanically anchored in a flexible substrate, and a cost-effective solution-based fabrication strategy for this new transparent electrode. The embedded nature of the metal-mesh electrodes provides a series of advantages, including surface smoothness that is crucial for device fabrication, mechanical stability under high bending stress, strong adhesion to the substrate with excellent flexibility, and favorable resistance against moisture, oxygen, and chemicals. The novel fabrication process replaces vacuum-based metal deposition with an electrodeposition process and is potentially suitable for high-throughput, large-volume, and low-cost production. In particular, this strategy enables fabrication of a high-aspect-ratio (thickness to linewidth) metal mesh, substantially improving conductivity without considerably sacrificing transparency. Various prototype flexible transparent electrodes are demonstrated with transmittance higher than 90% and sheet resistance below 1 ohm sq^{-1} , as well as extremely high figures of merit up to 1.5×10^4 , which are among the highest reported values in recent studies. Finally using our embedded metal-mesh electrode, a flexible transparent thin-film heater is demonstrated with a low power density requirement, rapid response time, and a low operating voltage.

A. Khan, C. Zhang, Dr. W.-D. Li
Department of Mechanical Engineering
The University of Hong Kong
Pokfulam, Hong Kong, China
E-mail: liwd@hku.hk

S. Lee, Prof. L. J. Guo
Department of Mechanical Engineering
The University of Michigan
Ann Arbor, MI 48109, USA

T. Jang, Prof. L. J. Guo
Department of Electrical Engineering and Computer Science
The University of Michigan
Ann Arbor, MI 48109, USA

Z. Xiong, Dr. J. Tang
Department of Chemistry
The University of Hong Kong
Pokfulam, Hong Kong, China

C. Zhang, Dr. W.-D. Li
HKU-Shenzhen Institute of Research and Innovation (HKU-SIRI)
Shenzhen, China

DOI: 10.1002/sml.201600309



1. Introduction

Transparent conductors are key components in optoelectronic devices^[1] such as displays,^[2] light-emitting diodes,^[3] touchscreens,^[4] solar cells,^[5] and smart windows.^[6] In addition to low sheet resistance and high optical transparency^[7] needed for conventional transparent conductors, emerging flexible optoelectronic devices also demand excellent flexibility^[1,8] in next-generation transparent electrodes. Currently, the dominant materials for transparent conductors are transparent conductive oxides (TCOs) such as indium tin oxide and fluorine-doped tin oxide (FTO). Although these materials have exhibited desirable performance, many concerns, including film brittleness,^[9] low infrared transmittance,^[10] low abundance,^[11] and inability of high temperature annealing on plastic substrates, limit their suitability for use in next-generation flexible optoelectronic devices.

New flexible transparent conductors that can overcome these limitations have been investigated.

Transparent conductors based on graphene,^[12] carbon nanotubes (CNTs),^[13] and conducting polymers^[14,15] have recently been introduced. Although the flexibility of these transparent conductors is greatly improved, their performance highly depends on the sample preparation and often does not meet the requirement for many applications regarding conductivity and stability.^[16] Furthermore, the high-throughput and large-area production of graphene, CNTs, and conducting polymers remains expensive and often energy-intensive.^[1] Substantial improvements in the manufacturing process must be achieved before these new conductors can be considered potential alternatives for the conventional TCO-based transparent conductors. Another promising class of transparent conductors is derived from random metal nanowire networks^[17,18] and regular metal meshes,^[19–24] which have demonstrated great potential in optical transparency, electrical conductivity, and mechanical flexibility. In particular, transparent electrodes created through the percolation of random silver nanowires have received strong interest because they can be dispersed in ink and printed in low-cost solution-based processing, which is desirable when forming electronic devices on large-area flexible substrates.^[25] Yet, silver nanowire networks suffer from several problems such as difficulty in achieving uniform nanowire distribution over the entire substrate and the delamination of the nanowires from a substrate.^[8] Furthermore, the randomly dispersed nanowire network cannot be used as prepared; an additional process is typically needed to remove the capping polymer around the nanowire and reduce junction resistance, either by bulk heating,^[26] selective welding,^[27] or other chemical modifications.^[28,29]

Compared with silver nanowire-based transparent electrodes, regular metal-mesh electrodes appear more promising. Their transmittance and electrical conductivity can be tuned in a wide range by changing the line width, line spacing, and metal thickness.^[22] Also, in contrast to the limited material choices for nanowires, various metallic materials can be used in regular metal-mesh-based electrodes to achieve different work functions and chemical properties for various applications.^[20] However, the widespread adoption of metal-mesh electrodes has been hindered by many challenges. First, fabricating metal-mesh transparent electrodes often involves the physical deposition of metal materials from the vapor phase, which requires expensive vacuum-based processing.^[20–22,30] Second, a thick layer of metal mesh on the substrate, as required to achieve sufficiently high conductivity in many applications, may easily cause electrical short circuiting.^[31–34] Third, the weak adhesion between the metal mesh and substrate surface results in poor reliability, particularly in highly flexible optoelectronic devices.^[8,24] Some recent work has been making progress to address these challenges. Embedding the silver colloidal nanoparticles in embossed trenches on a plastic film^[35] has been used for commercial production but few metals can easily form nanoparticles and the reduced conductivity of annealed nanoparticles also limits their performance. Electroless plating was used to fabricate solution-grown silver nanowire ordered arrays.^[36] However, this method can be used for very few metals and its scalability for production is also limited. The aforementioned limitations

call for new metal-mesh transparent electrode structures as well as improved and scalable fabrication methods for their production.

Here, we propose a new type of embedded metal-mesh transparent electrodes (EMTEs) with metal meshes not only embedded but also mechanically anchored in a flexible substrate. The structure of the new EMTEs allows the use of thick metal mesh for high conductivity without sacrificing surface smoothness. The thick embedded metal mesh is demonstrated to achieve a ratio of electrical conductivity to optical conductivity of more than 10^4 , among the highest of all reported transparent electrodes. The embedded structure also improves the EMTE's mechanical stability under high bending stress and its chemical stability in an ambient environment. To enable low-cost, scalable, and large-area EMTE production, we developed a new fabrication approach combining lithography, electrodeposition, and imprint transfer, completely free of vacuum processing. The fabricated EMTE exhibits superior figure of merit as compared with previous approaches. A flexible and transparent thin-film heater (FTTH) based on the EMTE was characterized and exhibited a rapid response, required low input power density, and operated at an ultralow voltage, clearly demonstrating the potential of our EMTE as a high-performance alternative transparent conductor.

2. Results and Discussion

2.1. Self-Anchoring and Embedding Structure of the Metal-Mesh Transparent Electrodes

As displayed in **Figure 1a**, the EMTE comprises a metal mesh embedded in a flexible substrate. The top surface of the metal mesh is on the same level as the substrate surface, featuring an overall smooth surface for following device fabrication. The lower part of the metal mesh has a wider lateral dimension than the upper part does and thus can be mechanically anchored in the substrate to provide mechanical stability. The dimensions of the metal mesh, namely the pitch p , linewidth w , and mesh thickness t , determine the EMTE's electrical conductivity and optical transmittance. Because these dimensional parameters can be tailored in the fabrication process, the EMTE could have a wide range of artificially designed properties to meet different device requirements and be constructed using a wide selection of metals and thermoplastic substrate materials.

2.2. Fabrication of EMTEs through Lithography, Electrodeposition, and Imprint Transfer

The excellent electrical and optical properties of EMTE were achieved by a combination of three well-developed fabrication processes, i.e. lithography, electrodeposition and imprint transfer. The fabrication process is schematically described in Figure 1 b–f. In a typical fabrication process, after a photoresist layer is spin-coated on a cleaned FTO glass substrate, a photolithography step is conducted to create a mesh

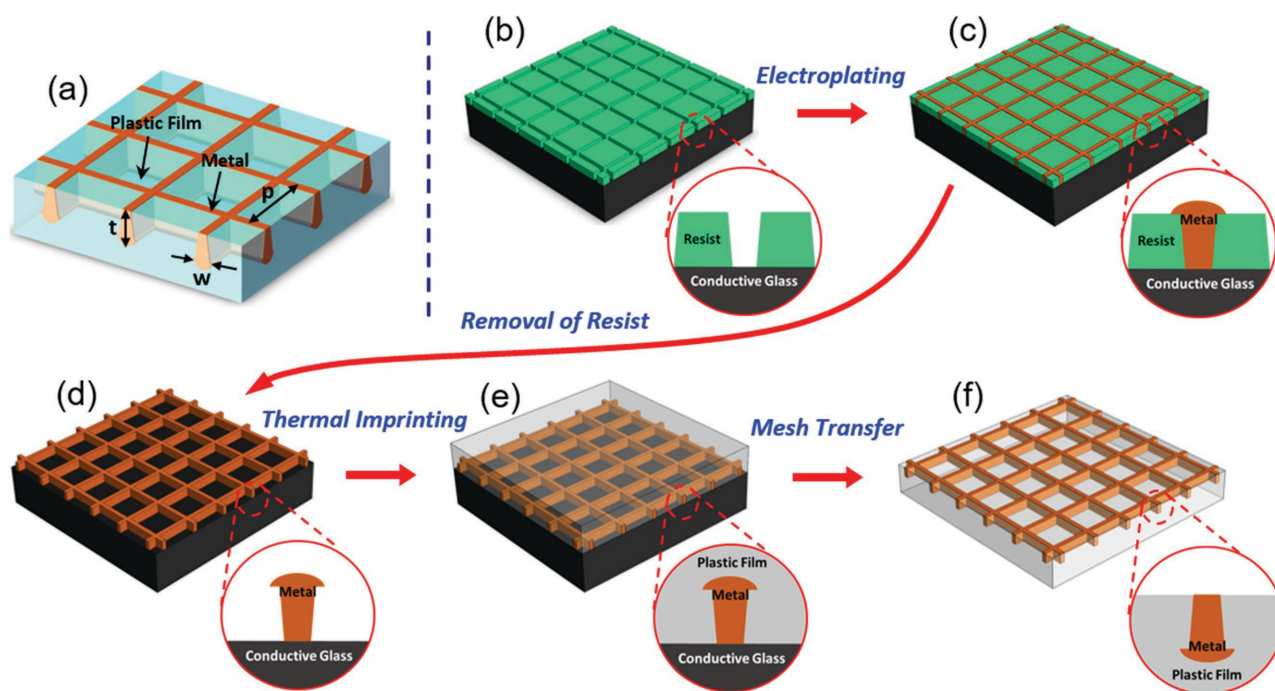


Figure 1. Schematic illustrations of a) the EMTE structure and b–f) its fabrication process. a) An EMTE with a metal mesh embedded in a transparent flexible plastic film. b) Mesh patterns formed in a resist layer coated on a conductive substrate by lithography. c) Electrodeposition of metal inside the resist trenches to form a uniform metal mesh. d) Removal of resist to obtain standing bare metal mesh on the conductive substrate. e) Heating and pressing the metal mesh into a plastic film. f) Peeling off the plastic film with the metal mesh transferred in a fully embedded form.

pattern in the photoresist through ultraviolet exposure and development (Figure 1b), exposing the FTO glass surface in the mesh trench. In addition to photolithography, other lithography methods, such as nanoimprint lithography,^[37] phase-shift photolithography^[38] and charged particle beam lithography,^[39] can also be applied in this step to obtain the resist template pattern. In the following electrodeposition step (Figure 1c), selected metal is deposited inside the lithographically defined trenches and fills the trenches with a uniform metal mesh. Next, the photoresist is gently dissolved in solvent, leaving the bare metal mesh on the surface of the FTO glass (Figure 1d). A thermoplastic film is then placed on the metal mesh and heated to above its glass transition temperature. A uniform pressure is applied to imprint the metal mesh into the softened plastic film (Figure 1e). Finally, after cooling the stack and separating the plastic film from the FTO glass, the metal mesh is transferred and embedded in the plastic film to complete the fabrication process (Figure 1f). The entire fabrication process is solution-based and performed in an ambient environment without any vacuum processing, and it can thus be readily adapted to large-volume production.

An EMTE with a copper mesh on a cyclic olefin copolymer (COC) film was fabricated through this process as a demonstration. Using copper in transparent electrodes is advantageous because of copper's low resistivity and high abundance. COC is selected as the substrate material because of its unique combination of beneficial properties (Table S1, Supporting Information) such as low water absorption, low surface energy, high strength, and high chemical resistance to acids and alkalis.^[40] COC exhibits particularly

favorable optical transparency extending into the near-UV range (Figure S1, Supporting Information), which is desirable in photovoltaic applications. Scanning electron microscopy (SEM) and atomic force microscopy (AFM) images in **Figure 2a–c** show the morphological characterization of the EMTE at different stages of the fabrication. Figure 2a displays the SEM and AFM images of the trench in the photoresist film created using photolithography (Figure 1b). On this sample, the photoresist trench had a 50 μm pitch, and its trench width and depth were ≈ 4 and 2 μm , respectively. Figure 2b presents the electroplated copper mesh on the FTO glass (Figure 1d). The copper mesh was deposited with a 5 mA current over a $2 \times 2 \text{ cm}^2$ area. As evident from the images, the copper mesh had linewidth and thickness of ≈ 4 and 1.8 μm , respectively. Figure 2c reveals that the copper mesh finally transferred onto a COC film (Figure 1f). The AFM characterization revealed that the surface roughness of the completed EMTE with a 1.8 μm mesh thickness was less than 50 nm, confirming its fully embedded structure.

The fabrication process was further investigated by changing the electrodeposition time to fabricate copper EMTEs of varying thickness, in which the electrodeposition current (5 mA) and substrate size ($2 \times 2 \text{ cm}^2$) are maintained constant. The relationship of metal thickness and electrodeposition time is summarized in Figure 2d. The curve indicates that metal thickness increases nonlinearly with electrodeposition time. This is due to the cross-section of the trench not being perfectly rectangular (Figure 2a); rather, it is narrower at the bottom. Therefore, during electrodeposition with a constant current, the rate of increase in deposited metal thickness (i.e., the slope of the curve in Figure 2d) decreases

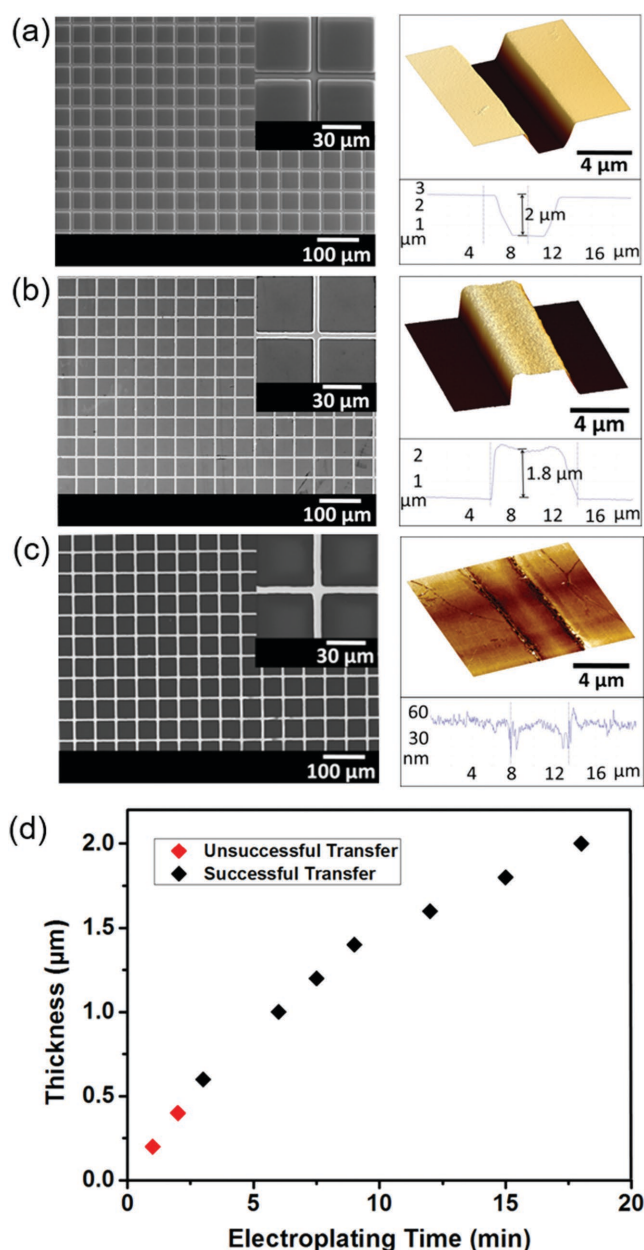


Figure 2. Fabrication of prototype 50 μm pitch copper EMTEs. Morphological characterization by SEM (left) and AFM (right) of an EMTE at different fabrication stages: a) as-developed mesh pattern in the photoresist; b) copper mesh on the FTO glass substrate after removal of photoresist; c) copper mesh transferred and fully embedded in a COC film. d) Plot of metal-mesh thickness versus electroplating time at a constant electrodeposition current (5 mA) and substrate size (2×2 cm). Cases of successful and unsuccessful subsequent imprint transfer are represented by black and red colors, respectively.

with time. Thus, the electrodeposited metal mesh has a larger width at the upper part, which is useful for imprint transfer because it can be mechanically anchored in the substrate. With a sufficiently long electrodeposition time, the overplating of metal out of the trench results in a slower increase rate of metal thickness and a further increased lateral dimension on the overplated cap, which was the case for the two samples with 15 and 18 min of electrodeposition time in Figure 2d. Detailed characterizations of these samples can

be found in the Supporting Information (Figure S2). After the removal of the photoresist template, these metal meshes were transferred to COC films through thermal imprinting. However, the transfer could be successful only for meshes thicker than 600 nm. The reason for the unsuccessful transfer was that the COC film trapping force applied on the sidewall of thinner metal meshes, including the interfacial friction and mechanical interlocking, could not counteract the adhesion force between the metal and FTO glass. Thus, the adhesion at the metal–FTO interface and the metal–COC interface as well as the geometric profile of the metal mesh are crucial to reliable fabrication of EMTEs.

2.3. Electrical and Optical Characterization of EMTEs

Our fabrication process allows easy control and variation of metal-mesh thickness while not considerably altering the lateral dimension of the metal mesh, providing a feasible method of improving the electrical conductivity of EMTEs without sacrificing their transmittance. **Figure 3a** provides the transmittance of typical copper EMTEs with thicknesses of 600 nm, 1 μm , and 2 μm in the 300–850 nm wavelength range. Only a marginal decrease in the transmittance over the measured spectral range was observed when metal-mesh thickness increased from 600 nm to 2 μm , and this decrease is attributable to the nonrectangular shape of the photoresist trench and overplating of metal. On the other hand, sheet resistance of EMTEs can be substantially reduced when the metal thickness is increased, as displayed in Figure 3b. An extremely low sheet resistance of 0.07 ohm sq^{-1} was observed for the 2 μm thick copper EMTE, and the transmittance at the 550 nm wavelength was still above 70%.

To gain further insight into how metal thickness affects the overall performance of the EMTE, a commonly used figure of merit (FoM), namely the ratio of electrical conductance to optical conductance ($\sigma_{\text{dc}}/\sigma_{\text{opt}}$), was calculated for all the EMTEs displayed in Figure 3b by using the following widely accepted expression^[15,18,21,22] (Equation (1))

$$\text{FoM} = \frac{\sigma_{\text{dc}}}{\sigma_{\text{opt}}} = \frac{188.5}{R_s \left(\frac{1}{\sqrt{T}} - 1 \right)} \quad (1)$$

where T is the optical transmittance at a wavelength of 550 nm and R_s is the sheet resistance. The inset of Figure 3b provides the plot of the FoM as a function of metal thickness. The presented data indicate that the metal thickness has a considerable effect on the sheet resistance and hence on the value of the FoM by increasing the electrical conductivity of a thicker metal mesh without substantially sacrificing transmittance. Our EMTE achieved FoM of more than 1.5×10^4 , which is among the highest such values ever reported. Figure 3c presents a comparison of our FoM with those of other transparent electrodes reported in recent studies. These data clearly indicate that our EMTE boasts superior overall performance compared with most existing metal meshes, metal nanowire and hybrid transparent

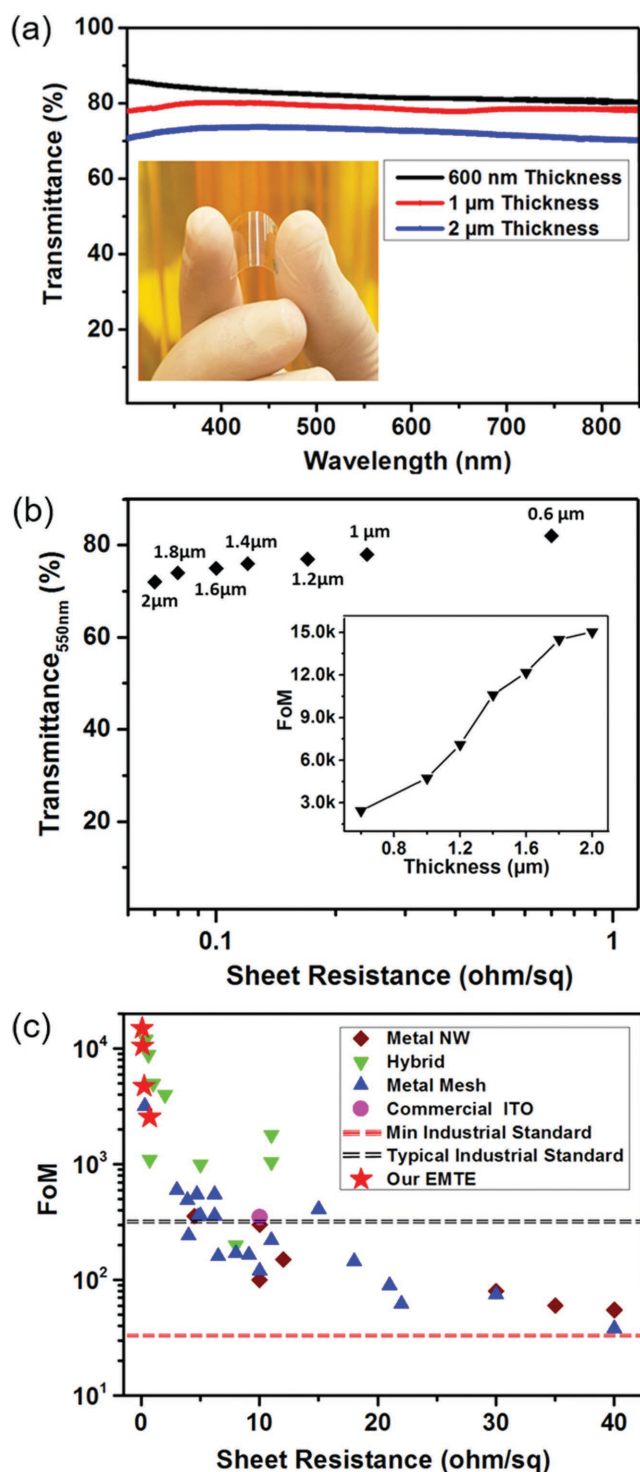


Figure 3. Performance characterization of the prototype 50 μm pitch copper EMTEs. a) UV-vis spectra of the representative copper EMTEs with thickness of 600 nm, 1 μm , and 2 μm , respectively. b) Plot of transmittance versus sheet resistance for copper EMTEs with different mesh thickness, with calculated FoMs shown in the inset. c) Comparison of the FoMs of EMTEs with other published transparent electrodes (metal NW,^[41–48] metal mesh,^[19–24,35,49–58] and hybrid^[59–63]) and industrial standards.^[63]

electrodes. Furthermore, measurement of the normalized transmittance at different incident angles shows negligible angle dependence up to 60° from the normal direction (Figure S3, Supporting Information).

2.4. Dimensional Scalability and Material Versatility

The proposed EMTE structure and the demonstrated fabrication process can be applied to metal meshes with sub-micrometer feature sizes, which benefit many optoelectronic applications by providing improved invisibility and continuity.^[20] To demonstrate the dimensional scalability, sub-micrometer-linewidth copper EMTEs were fabricated on COC films through the aforementioned process incorporating electron beam lithography (EBL) and a UV stepper, respectively. **Figure 4a–c** illustrates the morphological characterization of EBL-patterned EMTE fabrication at different stages. Figure 4a presents the SEM and AFM images of trenches created in a polymethyl methacrylate (PMMA) film by e-beam lithography. The trench width and depth were ≈ 400 and 150 nm, respectively. Figure 4b displays the copper mesh electroplated on the FTO glass (after the removal of the PMMA resist), and Figure 4c shows the imprint-transferred copper mesh on a COC film. The mesh on the COC film was in a fully embedded form, providing stability and strong adhesion with the polymer film. A UV stepper was also used in the patterning step to fabricate sub-micrometer-linewidth ($p = 50 \mu\text{m}$, $w = 800 \text{ nm}$, $t = 1.5 \mu\text{m}$) copper EMTEs on large area ($1.8 \times 1.8 \text{ cm}^2$) for electrical and optical characterization (Figure S4a–c, Supporting Information).

Figure 5a presents the UV-vis spectra and sheet resistance of this UV stepper fabricated EMTE. Due to the smaller linewidth, the sample demonstrates high optical transmittance (94% at 550 nm wavelength) with very low sheet resistance (0.61 ohm sq^{-1}). These successful fabrications confirmed that the EMTE structure and its key fabrication steps can be reliably scaled down to a sub-micrometer range. In fact, the electrodeposition and imprint-transfer processes allow an ultimate linewidth of metal mesh in the sub-100 nm range^[64] with a high aspect ratio, providing great potential of further reducing the linewidth of the EMTE mesh for better continuity and transmittance.

Increasing the gap size of the EMTE while maintaining same linewidth can also improve the transmittance. Figure 5b displays the UV-vis spectra and sheet resistance of a highly transparent copper EMTE on a $5 \times 5 \text{ cm}$ large COC substrate with a pitch of 150 μm and with a linewidth and metal-mesh thickness of 4 and 1 μm , respectively. Because of large line spacing, the sample exhibits high optical transmittance (94%) and retains low sheet resistance (0.93 ohm sq^{-1}), compared to the 78% transmittance and 0.24 ohm sq^{-1} sheet resistance of the previous copper EMTE with a 50 μm pitch. In similar fashion, various combinations of optical transparency and sheet resistance can be obtained for various applications by optimizing the geometric parameters of the metal mesh.

Another crucial advantage of our transparent electrodes over random nanowire-based transparent electrodes is the wide range of usable materials. To demonstrate that our fabrication is versatile regarding material choice, EMTEs of silver, gold, nickel, and zinc were also fabricated on COC films. Figure 5c presents the UV-vis transmittance spectra and sheet resistance of these EMTEs. The transmittance spectra were nearly flat and featureless over the entire visible region, which is advantageous for display devices and

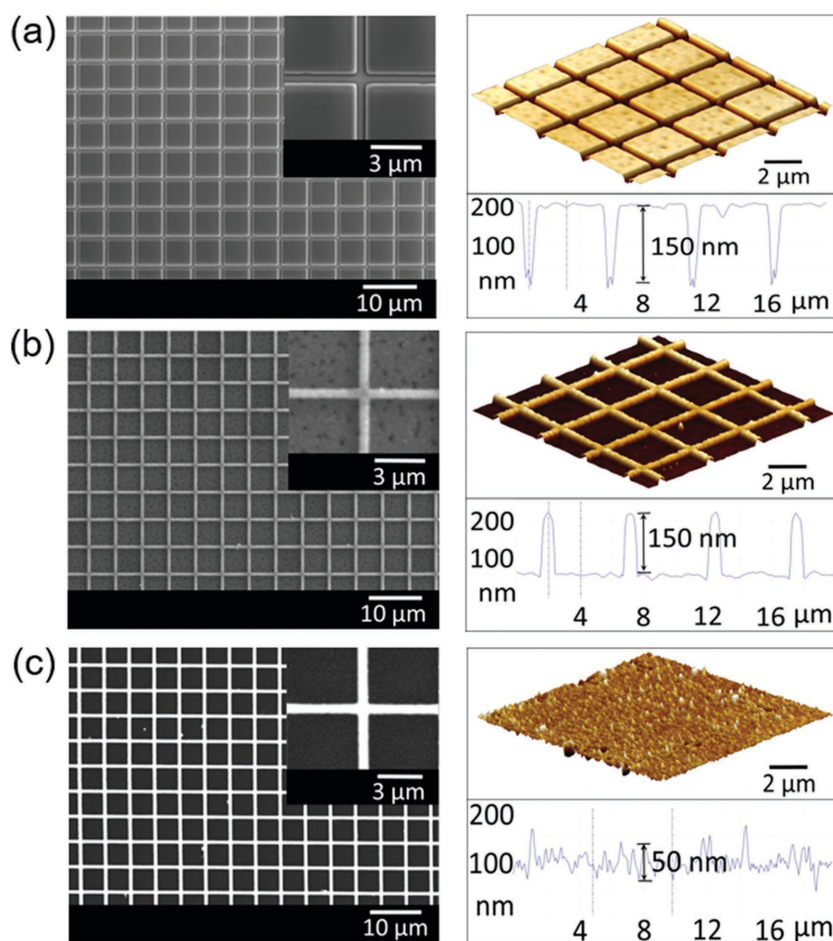


Figure 4. Morphological characterization by SEM (left) and AFM (right) of a prototype sub-micrometer-linewidth EMTE at different fabrication stages. a) Nanomesh patterns exposed in a PMMA resist film by electron beam lithography. b) Electroplated copper nanomesh on the FTO glass substrate after removal of PMMA resist. c) Copper nanomesh transferred and fully embedded in a COC film.

solar cell applications. Silver mesh-, nickel mesh-, and zinc mesh-based EMTEs had similar metal thickness; therefore, all three samples had nearly the same transmittance ($\approx 78\%$ at a 550 nm wavelength), whereas the sheet resistances were 0.52, 1.40, and 1.02 ohm sq^{-1} , respectively. Because of varying metal thickness, the copper mesh- and gold mesh-based EMTEs (≈ 600 and $2 \mu\text{m}$, respectively) had transmittances of 82% and 72% and sheet resistances of 0.70 and 0.20 ohm sq^{-1} , respectively. The sheet resistance values of all the EMTEs were in accordance with the electrical resistivity values of the respective metals (Table S2, Supporting Information). The successful fabrication of these prototype EMTEs validated the flexibility of material choice, thus fulfilling different requirements on the electrode's work function and chemical stability in different devices.

2.5. Mechanical and Environmental Stability

In addition to enhancing the electrical and optical performance of the EMTE, the embedded nature of the metal mesh greatly improves its adhesion with the substrate and

enhances its stability under bending, heating, and chemical attack. **Figure 6a,b** provides the test results of mechanical stability on copper EMTEs under cyclic tensile and compressive bending stress. Figure 6a presents the variation in sheet resistance as a function of the number of cycles for repeated compressive bending to radii of 5, 4, and 3 mm. The results clearly indicate that for 5 and 4 mm bending radii, no noticeable change in sheet resistance (0.07 ohm sq^{-1}) occurs for up to 1000 bending cycles. For a 3 mm bending radius, the change in sheet resistance is within 100% of its original value (from 0.07 ohm sq^{-1} to 0.13 ohm sq^{-1}). This remarkable copper mesh stability is attributable to its embedded nature. Similarly, for tensile loading, changes in sheet resistance versus the number of repeated bending cycles are displayed in Figure 6b, revealing that for 1000 repeated bendings to 5, 4, and 3 mm radii, the sheet resistances varied by $\approx 30\%$ (from 0.10 to 0.13 ohm sq^{-1}), 150% (from 0.10 to 0.25 ohm sq^{-1}), and 350% (from 0.10 to 0.45 ohm sq^{-1}), respectively. These higher increases in sheet resistances presumably arose because of metal-mesh cracking (Figure S5, Supporting Information) under high tensile stress, indicating that the metal mesh is more vulnerable to failure under tensile stress than compressive stress. Further studies are required to investigate the failure mechanisms of the metal mesh under various bending loads and their effects on the performance of

the EMTE and derived devices.

The mechanical stability of the EMTE was also confirmed using a repeated adhesive tape test. The sheet resistance of a typical copper EMTE was measured after every 10 peeling tests using polypropylene tape with acrylic adhesive and was found to be unchanged after 100 cycles (Figure S6, Supporting Information), confirming that the strong adhesion is due to the mechanical anchoring of the embedded metal mesh in the substrate. The environmental stability of the as-fabricated copper EMTEs was evaluated by dipping them in deionized (DI) water and isopropyl alcohol (IPA) and exposing them to high-humidity and high-temperature conditions (60°C , 85% relative humidity). Figure 6c shows that after 24 h, the sheet resistances and morphological structures of the EMTEs remained unchanged. This superior stability of the copper EMTEs was further confirmed by performing the Energy-dispersive X-ray spectroscopy (EDS) analysis on both as-fabricated copper EMTE (Figure S7, Supporting Information) and the treated copper EMTEs (Figures S8–S10, Supporting Information), which showed no noticeable increase of oxygen element on the copper mesh. The favorable environmental stability demonstrated in these tests

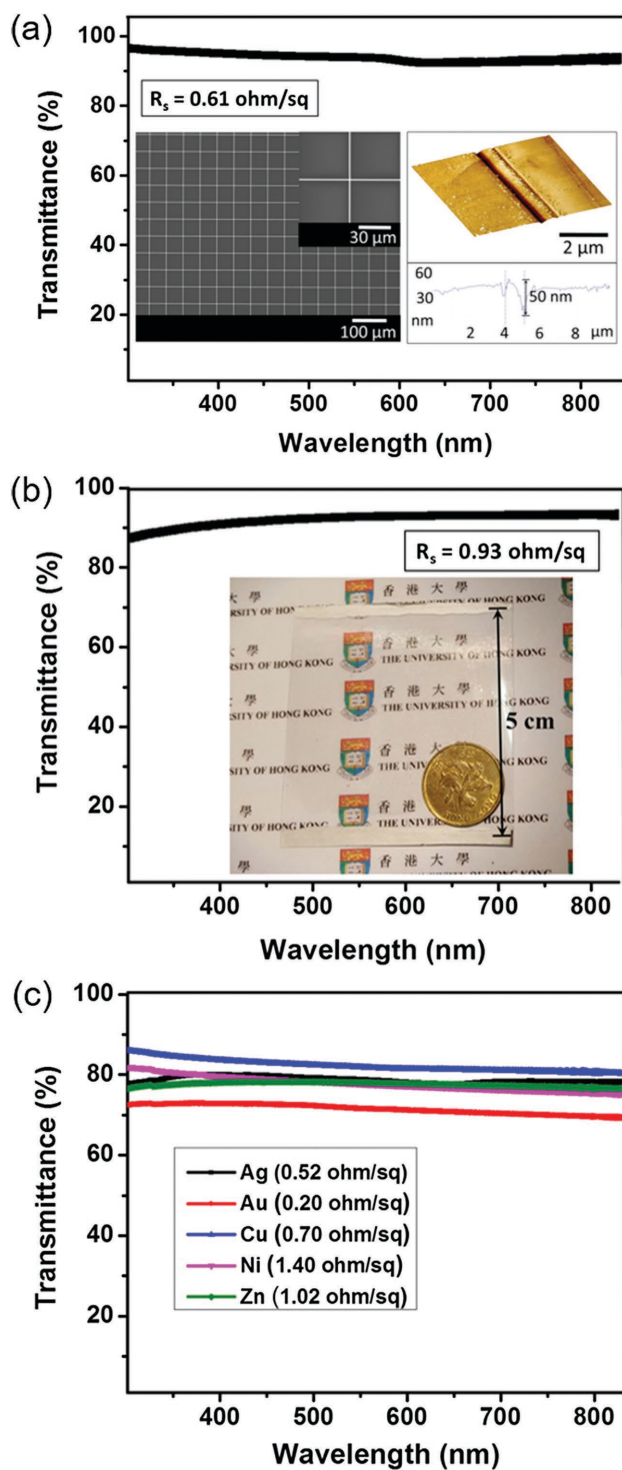


Figure 5. a) UV-vis spectra and sheet resistance of a highly transparent copper EMTE (50 μm pitch and 900 nm linewidth) on COC film; the insets show the SEM and AFM images of the final structure. b) UV-vis spectra and sheet resistance of a highly transparent copper EMTE with a 150 μm pitch on a 5×5 cm large COC film, with the optical image shown in the inset. c) UV-vis spectra and sheet resistances of 50 μm pitch EMTEs fabricated with various metals showing versatile material choices.

can also be attributed to the embedded nature of the EMTE and the chemical stability of the COC films that isolate and protect the metal mesh.

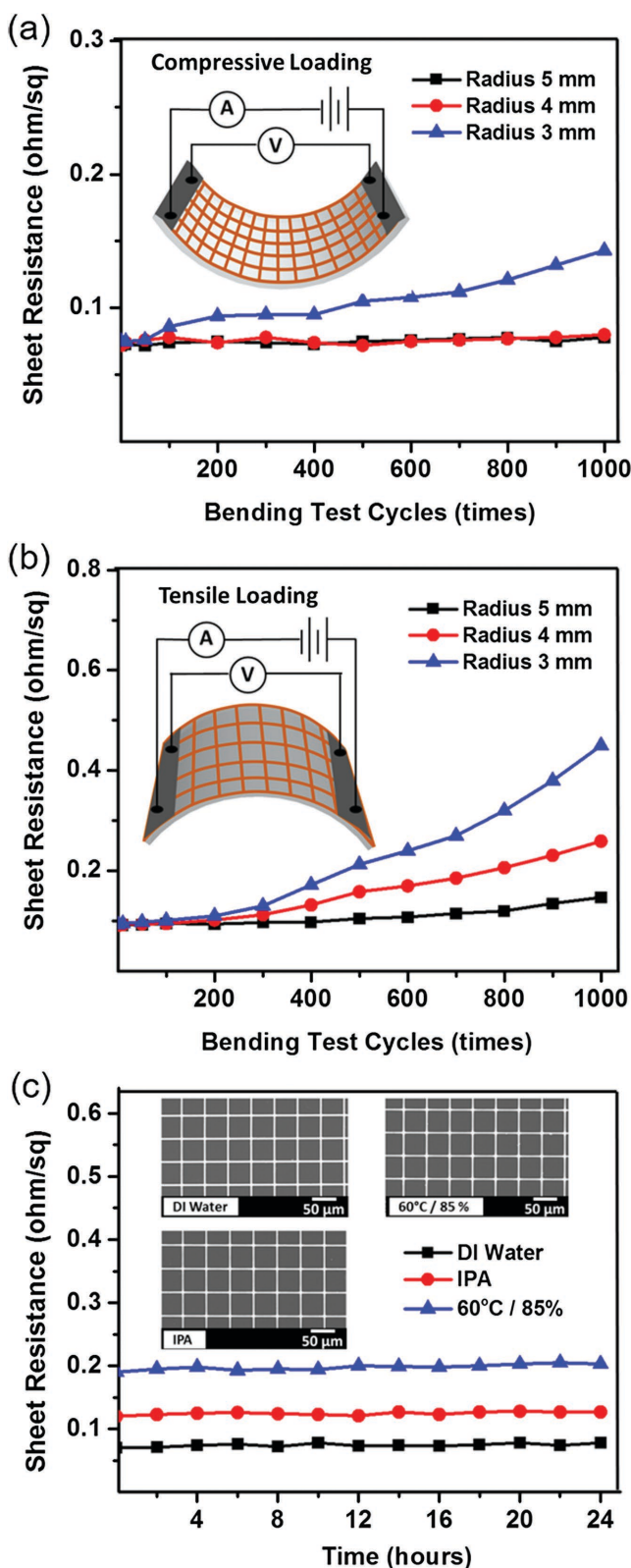


Figure 6. Mechanical stability of the copper EMTEs. a) Plot of variations in sheet resistance versus the number of cycles of repeated bending (compressive loading) to radii of 5, 4, and 3 mm, respectively. b) Plot of variations in sheet resistance versus the number of cycles of repeated bending (tensile loading) to radii of 5, 4, and 3 mm, respectively. c) Variations in sheet resistance during the chemical and environmental stability tests. Inset: SEM images after the tests.

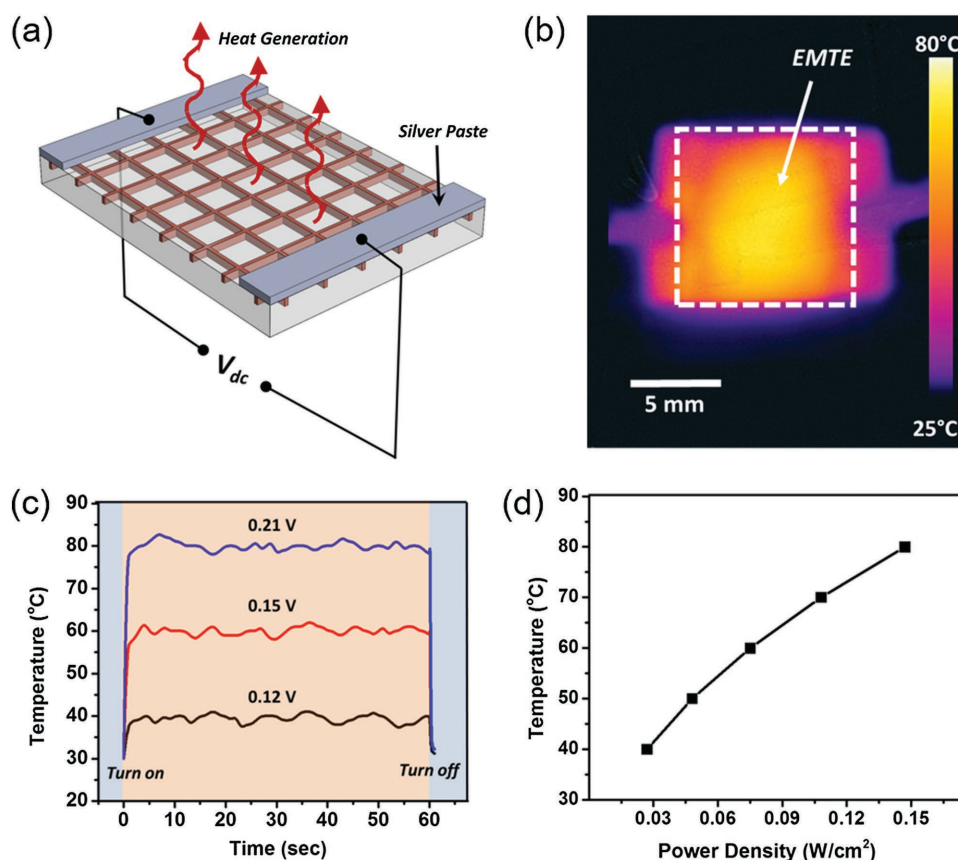


Figure 7. Demonstration of EMTE-based FTTH. a) Schematic illustration. b) Infrared thermal image showing uniform temperature distribution over the entire FTTH during operation. c) Plot of the temperature at FTTH center versus time at various applied voltages. d) Plot of the FTTH temperature at steady state versus calculated input power density.

2.6. Flexible Thin-Film Transparent Heater Using EMTEs

We constructed a transparent and flexible thin-film heater as a practical application of our EMTE, as schematically illustrated in **Figure 7a**. FTTHs have various applications such as in outdoor panel displays, window defrosters, liquid crystal display panels for harsh environments, periscopes, and thermal-based sensors.^[65–68] An FTTH's structure and principle are simple, but its high-performance operation with a low voltage, high transmittance, and rapid response can be achieved only with a superior transparent electrode. In our device, the DC voltage was supplied to the thin-film heater through silver paste contacts at the film edge, and the temperature of the film was monitored using an infrared thermal imaging camera. Figure 7b is a representative steady-state thermal image of a 1×1 cm FTTH with a sheet resistance of 0.3 ohm sq^{-1} and which is powered by an applied voltage of 0.21 V.

As the figure shows, the temperature distribution is rather homogeneous; this is due to the excellent thermal and electrical conductivity of our EMTE. The time-dependent temperature change of the heater is experimentally measured under various applied voltages from 0.12 to 0.21 V, as displayed in Figure 7c. Regardless of the input voltages, the steady-state temperature of the FTTH was reached within 2 s, demonstrating the rapid response of the device. The center temperature of the FTTH reached 80 °C under 0.21 V

and the power density was calculated to be $\approx 0.15 \text{ W cm}^{-2}$ (Figure 7d), confirming its operation at low input voltages and with a low power density requirement, which is mainly because of the low sheet resistance of our EMTE. Accurate control of the FTTH temperature was achieved by adjusting the supplied voltage, as demonstrated in Figure 7c. The video (Supporting Information Movie S1) displays the temperature distribution of the FTTH when tuning the supplied voltage. Compared with most published results,^[54,65–72] a lower power density requirement ($< 0.15 \text{ W cm}^{-2}$), a rapid response (< 2 s), and a lower operating voltage (< 1 V) make our EMTE-based FTTH to be a unique device for broad applications.

3. Conclusions

In summary, we proposed and demonstrated a new type of EMTEs with superior electrical conductivity and optical transmittance. $\sigma_{\text{dc}}/\sigma_{\text{opt}}$ values as high as 1.5×10^4 have been demonstrated on prototype copper EMTEs. Because of the electrode's embedded nature, excellent mechanical, chemical, and environmental stability were observed. Moreover, we developed a solution-processed fabrication approach that potentially could be adapted for the high-throughput and low-cost manufacturing of the proposed EMTE. This fabrication process has been demonstrated to be able to scale

for a larger EMTE area, narrower metal-mesh linewidths, and a wide range of materials. The approach can be easily adapted to make flexible and even stretchable devices.^[73] A transparent and flexible thin-film heater was constructed with this EMTE and demonstrated excellent performance compared with existing products. With superior performance and a low-cost, high-throughput fabrication process, our EMTE has broad applications in flexible optoelectronic devices.

4. Experimental Section

Photolithography-Based Fabrication of the EMTE: FTO glass substrates ($\approx 15 \text{ ohm sq}^{-1}$, South China Xiang S&T, China) were cleaned with a cotton swab and liquid detergent, rinsed thoroughly with another cotton swab and DI water, and then further cleaned by ultrasonication in isopropanol and DI water for 30 s before being dried with compressed air. AZ 1500 (Clariant, Switzerland) photoresist was spin-coated at 4000 rpm for 60 s to reach a film thickness of 1.8 μm on the cleaned FTO glass. It was then baked on a hotplate at 100 °C for 50 s. Thereafter, the photoresist was exposed using a URE-2000/35 UV mask aligner (Chinese Academy of Sciences, China) for an exposure dose of 20 mJ cm^{-2} . The photoresist was then developed in a AZ 300 MIF developer (Clariant, Switzerland) for 50 s. The samples were finally rinsed in DI water and blow-dried with compressed air.

A subsequent electrodeposition process used commercial aqueous copper, silver, gold, nickel, and zinc plating solutions (Caswell, USA). A Keithley 2400 SourceMeter was used to supply a constant 5 mA current to a two-electrode electrodeposition setup with the photoresist-covered FTO glass as the working electrode and metal bar as the counter electrode. Electrodeposition time was varied to achieve the desired thickness of deposited metal. After the electrodeposition was completed, the sample was thoroughly rinsed with distilled water, blow-dried with compressed air, and then placed in acetone for 5 min to remove the photoresist, leaving the bare metal mesh on the FTO glass substrate.

The metal mesh was then transferred to a 100 μm thick COC film (Grade 8007, TOPAS, Germany) by thermal imprint using a home-built setup consisting of a hydraulic press (Specac Ltd., UK), electrically heated platens with a temperature controller (Specac Ltd., UK), and a chiller (Grant Instruments, UK). During the thermal imprint process, the plates were heated to 100 °C and an imprinting pressure of 15 MPa was applied, holding it for 5 min. The heated platens were then cooled to the demolding temperature of 40 °C. Finally, the COC film was peeled from the conductive glass, with the metal mesh fully embedded in the COC film.

Fabrication of Sub-Micrometer EMTE Using EBL and UV Stepper: In the EBL fabrication, a positive-tone e-beam resist PMMA solution (15k M.W., 4 wt% in anisole) was first spin-coated at 2500 rpm for 60 s onto a cleaned FTO glass substrate and baked on a hotplate at 170 °C for 30 min. The mesh pattern was then written using a Philips FEI XL30 scanning electron microscope equipped with a JC Nabity pattern generator. The resist was then developed in a mixed solution of isopropanol and methyl isopropyl ketone at a 3:1 ratio for 1 min.

In the UV stepper fabrication, ITO coated glass substrates (Delta Technologies Ltd. $R_s = 10 \text{ ohm sq}^{-1}$) were first cleaned and a layer of positive photoresist (Dow Megaposit SPR 220–3.0) was spin-coated

at 5000 rpm for 30 s to achieve a thickness of 2 μm . Following a soft baking at 115 °C for 1 min, an i-line stepper (GCA AS200 AutoStep) was used for patterning sub-micrometer mesh patterns. The photoresist was then developed in AZ MIF-300 developer for 1 min. The samples were then rinsed in water and dried with nitrogen gas.

Performance Measurements: The morphology of the samples was characterized using an S-3400N scanning electron microscope (Hitachi, Japan) and a Multimode-8 atomic force microscope (Bruker, USA). The sheet resistance of the EMTE samples was measured using the four-probe method to eliminate contact resistance. During the measurement, four probes were placed on two silver paste-covered edges of a square sample, and the resistance was recorded with a Keithley 2400 SourceMeter (Keithley, USA). Optical transmission spectra were recorded using a Lambda 25 UV–vis spectrometer (Perkin Elmer, USA). All transmittance values presented in this paper are normalized to the absolute transmittance through the bare COC film substrate. EDS analysis was performed by S-3400N scanning electron microscope (Hitachi, Japan). For FTTH application, the DC voltage was supplied by the Keithley 2400 as a DC power supply to the heater through a silver contact at the film edge. The temperature of the film was measured using an FLIR ONE infrared thermal imager (FLIR Systems, USA).

Acknowledgements

This work was partially supported by the Young Scholar Program (61306123) of the National Natural Science Foundation of China, the Early Career Scheme of the Research Grants Council of the Hong Kong Special Administrative Region (Award No. 27205515), the Basic Research Program-General Program (JCYJ20140903112959959) from the Science and Technology Innovation Commission of Shenzhen Municipality, and the Seed Funding Programme for Basic Research (201411159212) of the University of Hong Kong. S.E.L., T.H.J., and L.J.G. acknowledge the support from the US National Science Foundation, Grant No. CMMI 1025020. The authors would like to thank Y.-T. Huang and S. P. Feng for UV–vis measurement.

- [1] D. S. Hecht, L. Hu, G. Irvin, *Adv. Mater.* **2011**, 23, 1482.
- [2] P. Blake, P. D. Brimicombe, R. R. Nair, T. J. Booth, D. Jiang, F. Schedin, L. A. Ponomarenko, S. V. Morozov, H. F. Gleeson, E. W. Hill, A. K. Geim, K. S. Novoselov, *Nano Lett.* **2008**, 8, 1704.
- [3] J. Wu, M. Agrawal, H. A. Becerril, Z. Bao, Z. Liu, Y. Chen, P. Peumans, *ACS Nano* **2010**, 4, 43.
- [4] J. Wang, M. Liang, Y. Fang, T. Qiu, J. Zhang, L. Zhi, *Adv. Mater.* **2012**, 24, 2874.
- [5] Z. Yu, L. Li, Q. Zhang, W. Hu, Q. Pei, *Adv. Mater.* **2011**, 23, 4453.
- [6] S. K. Deb, S. Lee, C. E. Tracy, J. R. Pitts, B. A. Gregg, H. M. Branz, *Electrochim. Acta* **2001**, 46, 2125.
- [7] R. G. Gordon, *MRS Bull.* **2000**, 25, 52.
- [8] K. Ellmer, *Nat. Photonics* **2012**, 6, 809.
- [9] D. R. Cairns, R. P. Witte, D. K. Sparacin, S. M. Sachsman, D. C. Paine, G. P. Crawford, R. R. Newton, *Appl. Phys. Lett.* **2000**, 76, 1425.
- [10] R. Bel Hadj Tahar, T. Ban, Y. Ohya, Y. Takahashi, *J. Appl. Phys.* **1998**, 83, 2631.
- [11] A. Kumar, C. Zhou, *ACS Nano* **2010**, 4, 11.

- [12] F. Bonaccorso, Z. Sun, T. Hasan, A. C. Ferrari, *Nat. Photonics* **2010**, 4, 611.
- [13] M. Zhang, S. Fang, A. A. Zakhidov, S. B. Lee, A. E. Aliev, C. D. Williams, K. R. Atkinson, R. H. Baughman, *Science* **2005**, 309, 1215.
- [14] S. Kirchmeyer, K. Reuter, *J. Mater. Chem.* **2005**, 15, 2077.
- [15] M. Vosgueritchian, D. J. Lipomi, Z. Bao, *Adv. Funct. Mater.* **2012**, 22, 421.
- [16] D. S. Hecht, R. B. Kaner, *MRS Bull.* **2011**, 36, 749.
- [17] S. De, T. M. Higgins, P. E. Lyons, E. M. Doherty, P. N. Nirmalraj, W. J. Blau, J. J. Boland, J. N. Coleman, *ACS Nano* **2009**, 3, 1767.
- [18] J. van de Groep, P. Spinelli, A. Polman, *Nano Lett.* **2012**, 12, 3138.
- [19] S. Hong, J. Yeo, G. Kim, D. Kim, H. Lee, J. Kwon, H. Lee, P. Lee, S. H. Ko, *ACS Nano* **2013**, 7, 5024.
- [20] H. Wu, D. Kong, Z. Ruan, P.-C. Hsu, S. Wang, Z. Yu, T. J. Carney, L. Hu, S. Fan, Y. Cui, *Nat. Nanotechnol.* **2013**, 8, 421.
- [21] B. Han, K. Pei, Y. Huang, X. Zhang, Q. Rong, Q. Lin, Y. Guo, T. Sun, C. Guo, D. Carnahan, M. Giersig, Y. Wang, J. Gao, Z. Ren, K. Kempa, *Adv. Mater.* **2014**, 26, 873.
- [22] H.-J. Kim, S.-H. Lee, J. Lee, E.-S. Lee, J.-H. Choi, J.-H. Jung, J.-Y. Jung, D.-G. Choi, *Small* **2014**, 10, 3767.
- [23] S. Kiruthika, R. Gupta, K. D. M. Rao, S. Chakraborty, N. Padmavathy, G. U. Kulkarni, *J. Mater. Chem. C* **2014**, 2, 2089.
- [24] H.-J. Choi, S. Choo, P.-H. Jung, J.-H. Shin, Y.-D. Kim, H. Lee, *Nanotechnology* **2015**, 26, 055305.
- [25] J. Jiu, M. Nogi, T. Sugahara, T. Tokuno, T. Araki, N. Komoda, K. Suganuma, H. Uchida, K. Shinozaki, *J. Mater. Chem.* **2012**, 22, 23561.
- [26] L. Hu, H. S. Kim, J.-Y. Lee, P. Peumans, Y. Cui, *ACS Nano* **2010**, 4, 2955.
- [27] E. C. Garnett, W. Cai, J. J. Cha, F. Mahmood, S. T. Connor, M. G. Christoforo, Y. Cui, M. D. McGehee, M. L. Brongersma, *Nat. Mater.* **2012**, 11, 241.
- [28] R. Zhu, C.-H. Chung, K. C. Cha, W. Yang, Y. B. Zheng, H. Zhou, T.-B. Song, C.-C. Chen, P. S. Weiss, G. Li, Y. Yang, *ACS Nano* **2011**, 5, 9877.
- [29] C.-H. Chung, T.-B. Song, B. Bob, R. Zhu, Y. Yang, *Nano Res.* **2012**, 5, 805.
- [30] C. Bao, J. Yang, H. Gao, F. Li, Y. Yao, B. Yang, G. Fu, X. Zhou, T. Yu, Y. Qin, J. Liu, Z. Zou, *ACS Nano* **2015**, 9, 2502.
- [31] T. H. J. van Osch, J. Perelaer, A. W. M. de Laat, U. S. Schubert, *Adv. Mater.* **2008**, 20, 343.
- [32] B. Y. Ahn, E. B. Duoss, M. J. Motala, X. Guo, S.-I. Park, Y. Xiong, J. Yoon, R. G. Nuzzo, J. A. Rogers, J. A. Lewis, *Science* **2009**, 323, 1590.
- [33] A. Khan, K. Rahman, M.-T. Hyun, D.-S. Kim, K.-H. Choi, *Appl. Phys. A* **2011**, 104, 1113.
- [34] A. Khan, K. Rahman, D. S. Kim, K. H. Choi, *J. Mater. Process. Technol.* **2012**, 212, 700.
- [35] L. Zhou, H.-Y. Xiang, S. Shen, Y.-Q. Li, J.-D. Chen, H.-J. Xie, I. A. Goldthorpe, L.-S. Chen, S.-T. Lee, J.-X. Tang, *ACS Nano* **2014**, 8, 12796.
- [36] B. Sciacca, J. van de Groep, A. Polman, E. C. Garnett, *Adv. Mater.* **2015**, 28, 905.
- [37] S. Y. Chou, P. R. Krauss, P. J. Renstrom, *Appl. Phys. Lett.* **1995**, 67, 3114.
- [38] K. M. Kyu, G. O. Jong, L. J. Yong, L. J. Guo, *Nanotechnology* **2012**, 23, 344008.
- [39] V. R. Manfrinato, L. Zhang, D. Su, H. Duan, R. G. Hobbs, E. A. Stach, K. K. Berggren, *Nano Lett.* **2013**, 13, 1555.
- [40] A. Khan, S. Li, X. Tang, W.-D. Li, *J. Vac. Sci. Technol., B* **2014**, 32, 06F02.
- [41] A. R. Rathmell, S. M. Bergin, Y.-L. Hua, Z.-Y. Li, B. J. Wiley, *Adv. Mater.* **2010**, 22, 3558.
- [42] H. Wu, L. Hu, M. W. Rowell, D. Kong, J. J. Cha, J. R. McDonough, J. Zhu, Y. Yang, M. D. McGehee, Y. Cui, *Nano Lett.* **2010**, 10, 4242.
- [43] Z. Yu, Q. Zhang, L. Li, Q. Chen, X. Niu, J. Liu, Q. Pei, *Adv. Mater.* **2011**, 23, 664.
- [44] J. Lee, P. Lee, H. Lee, D. Lee, S. S. Lee, S. H. Ko, *Nanoscale* **2012**, 4, 6408.
- [45] T. Tokuno, M. Nogi, J. Jiu, T. Sugahara, K. Suganuma, *Langmuir* **2012**, 28, 9298.
- [46] D. Zhang, R. Wang, M. Wen, D. Weng, X. Cui, J. Sun, H. Li, Y. Lu, *J. Am. Chem. Soc.* **2012**, 134, 14283.
- [47] H. Guo, N. Lin, Y. Chen, Z. Wang, Q. Xie, T. Zheng, N. Gao, S. Li, J. Kang, D. Cai, D.-L. Peng, *Sci. Rep.* **2013**, 3, 2323.
- [48] J. Wang, C. Yan, W. Kang, P. S. Lee, *Nanoscale* **2014**, 6, 10734.
- [49] M. G. Kang, L. J. Guo, *Adv. Mater.* **2007**, 19, 1391.
- [50] M.-G. Kang, M.-S. Kim, J. Kim, L. J. Guo, *Adv. Mater.* **2008**, 20, 4408.
- [51] J. Zou, H.-L. Yip, S. K. Hau, A. K.-Y. Jen, *Appl. Phys. Lett.* **2010**, 96, 203301.
- [52] J. Yonghee, K. Jihoon, B. Doyoung, *J. Phys. D: Appl. Phys.* **2013**, 46, 155103.
- [53] C. F. Guo, T. Sun, Q. Liu, Z. Suo, Z. Ren, *Nat. Commun.* **2014**, 5, 3121.
- [54] R. Gupta, K. D. M. Rao, K. Srivastava, A. Kumar, S. Kiruthika, G. U. Kulkarni, *ACS Appl. Mater. Interfaces* **2014**, 6, 13688.
- [55] T. Iwahashi, R. Yang, N. Okabe, J. Sakurai, J. Lin, D. Matsunaga, *Appl. Phys. Lett.* **2014**, 105, 223901.
- [56] S. Kiruthika, K. D. M. Rao, K. Ankush, G. Ritu, G. U. Kulkarni, *Mater. Res. Express* **2014**, 1, 026301.
- [57] J. H. Park, D. Y. Lee, Y.-H. Kim, J. K. Kim, J. H. Lee, J. H. Park, T.-W. Lee, J. H. Cho, *ACS Appl. Mater. Interfaces* **2014**, 6, 12380.
- [58] W.-K. Kim, S. Lee, D. H. Lee, I. H. Park, J. S. Bae, T. W. Lee, J.-Y. Kim, J. H. Park, Y. C. Cho, C. R. Cho, S.-Y. Jeong, *Sci. Rep.* **2015**, 5, 10715.
- [59] P.-C. Hsu, S. Wang, H. Wu, V. K. Narasimhan, D. Kong, H. Ryoung Lee, Y. Cui, *Nat. Commun.* **2013**, 4, 2522.
- [60] J. G. Ok, M. K. Kwak, C. M. Huard, H. S. Youn, L. J. Guo, *Adv. Mater.* **2013**, 25, 6554.
- [61] B. W. An, B. G. Hyun, S.-Y. Kim, M. Kim, M.-S. Lee, K. Lee, J. B. Koo, H. Y. Chu, B.-S. Bae, J.-U. Park, *Nano Lett.* **2014**, 14, 6322.
- [62] W. Bao, J. Wan, X. Han, X. Cai, H. Zhu, D. Kim, D. Ma, Y. Xu, J. N. Munday, H. D. Drew, M. S. Fuhrer, L. Hu, *Nat. Commun.* **2014**, 5, 4224.
- [63] T. Gao, Z. Li, P.-s. Huang, G. J. Shenoy, D. Parobek, S. Tan, J.-k. Lee, H. Liu, P. W. Leu, *ACS Nano* **2015**, 9, 5440.
- [64] M. J. Burek, J. R. Greer, *Nano Lett.* **2010**, 10, 69.
- [65] Y. H. Yoon, J. W. Song, D. Kim, J. K. Park, S. K. Oh, C. S. Han, *Adv. Mater.* **2007**, 19, 4284.
- [66] J. Kang, H. Kim, K. S. Kim, S.-K. Lee, S. Bae, J.-H. Ahn, Y.-J. Kim, J.-B. Choi, B. H. Hong, *Nano Lett.* **2011**, 11, 5154.
- [67] D. Sui, Y. Huang, L. Huang, J. Liang, Y. Ma, Y. Chen, *Small* **2011**, 7, 3186.
- [68] T. Kim, Y. W. Kim, H. S. Lee, H. Kim, W. S. Yang, K. S. Suh, *Adv. Funct. Mater.* **2013**, 23, 1250.
- [69] H.-S. Jang, S. K. Jeon, S. H. Nahm, *Carbon* **2011**, 49, 111.
- [70] C. Celle, C. Mayousse, E. Moreau, H. Basti, A. Carella, J.-P. Simonato, *Nano Res.* **2012**, 5, 427.
- [71] D. Kim, L. Zhu, D.-J. Jeong, K. Chun, Y.-Y. Bang, S.-R. Kim, J.-H. Kim, S.-K. Oh, *Carbon* **2013**, 63, 530.
- [72] Q. Huang, W. Shen, X. Fang, G. Chen, J. Guo, W. Xu, R. Tan, W. Song, *RSC Adv.* **2015**, 5, 45836.
- [73] T.-H. Jang, C. Zhang, H.-S. Youn, J. Zhou, L. J. Guo, *IEEE Trans. Antennas Propag.* **2015**, in review.

Received: January 29, 2016
 Revised: February 24, 2016
 Published online: